NUCL SCI TECH (2018) 29:3
https://doi.org/10.1007/s41365-017-0339-z

Gamma and X-ray radiation compatibility of Ti–Ta–Hf–Zr alloys used for coronary stent applications

L. Seenappa[1,2,4] · H. C. Manjunatha[1,4] · K. N. Sridhar[2,4] · Chikka Hanumantharayappa[3,4]

Received: 21 June 2017 / Revised: 21 June 2017 / Accepted: 6 October 2017 / Published online: 21 December 2017

Abstract We have studied the gamma and X-ray radiation compatibility of Ti-based alloys such as Ti–37Ta–26Hf–13Zr-24 (wt%) [Alloy 1], Ti–40Ta–22Hf–11.7Zr-26.3 (wt%) [Alloy 2], Ti–45Ta–18.4Hf–10Zr-26.6 (wt%) [Alloy 3], Ti–50Ta–15Hf–8Zr-27 (wt%) [Alloy 4], Ti–55Ta–12Hf–7Zr-26 (wt%) [Alloy 5], and Ti–60Ta–10Hf–5Zr-25 (wt%) [Alloy 6]. Gamma and X-ray radiation compatibility is studied by evaluating the mass attenuation coefficient, mean free path, HVL, TVL effective atomic number, effective electron density, exposure buildup factor, and relative dose. We have compared these parameters for studied alloys with that of arteries. The alloys Ti–55Ta–12Hf–7Zr-26 and Ti–60Ta–10Hf–5Zr-25 have added properties such as gamma/X-ray radiation compatibility, high elastic admissible strain, high mechanical strength, and excellent biocompatibility. Hence, we may suggest that, among Ti–Ta–Hf–Zr alloys, these alloys are best materials for coronary stent applications.

Keywords Stentalloys · X-ray · Gamma · Mass attenuation coefficient

✉ L. Seenappa
seenappakolar@gmail.com

1 Department of Physics, Government College for Women, Kolar, Karnataka 563101, India

2 Department of Physics, Government First Grade College, Kolar, Karnataka 563101, India

3 Vivekananda Degree College, Bangalore, Karnataka 560 055, India

4 Research and Development Centre, Bharathiar University, Coimbatore 641046, India

1 Introduction

Ti-based alloys are widely used in the biomedical application. Vasilescu et al. [1] studied the microstructure, surface characterization, and long-term stability of the Ti–Zr–Ta–Ag alloy for implant use. Sreenivasa Reddy and Kanchana [2] studied the dynamical properties such as pressure and temperature effects on ternary Ni-based Ti, V, Zr, Nb, Hf, and Ta alloys. Zheng et al. [3] investigated the effect of Zr content on the thermal stability of a Ti–Ta alloy. Patrik Stenlund et al. [4] developed a Ti–Ta–Nb–Zr alloy to use implant material for bone and teeth. Xu et al. [5] studied the corrosion behavior of the Ti–Nb–Ta–Zr–Fe alloy for biomedical applications. Ma and Sun [6] studied the characterization of biomedical Ti–Nb–Ta–Zr alloy. Zhang et al. [7] investigated the microstructures, phase transformations, mechanical properties, and shape memory effect of Ti–Zr–Nb–Al alloys. Kim et al. [8] investigated the hydroxyapatite formation on biomedical Ti–Ta–Zr alloys by magnetron sputtering and electrochemical deposition. Song et al. [9] studied the microstructure and fatigue behaviors of a biomedical Ti–Nb–Ta–Zr alloy containing trace amounts of CeO_2. Wei et al. [10] investigated the effects of oxygen concentration on the microstructure and thermal expansion properties of Ti–Nb–Zr–Ta–O alloys. Elias et al. [11] studied the microstructural and mechanical characterization of biomedical Ti–Nb–Ta–Zr and Ti–Nb–Zr alloys. Jeong et al. [12] studied the control of nanotube shape and morphology on Ti–Nb(Ta)–Zr alloys. Sakaguchi et al. [13] studied the relationships between tensile deformation behavior and microstructure in Ti–Nb–Ta–Zr system alloys. Málek et al. [14] studied the influence of chemical composition and thermo-mechanical treatment on Ti–Nb–Ta–Zr alloys. Xu et al. [15] investigated the effects of cold deformation on the microstructure, texture evolution, and mechanical properties of the Ti–Nb–Ta–Zr–Fe alloy. Wei et al. [16] studied the influence of oxygen content on microstructure and mechanical properties of a Ti–Nb–Ta–Zr alloy. Vasilescu et al. [17] proposed a new Ti–Zr–Ta–Ag alloy for biomedical applications.

At present, the most commonly used stent materials include metal and polymer materials. Metallic stents exhibit a more stable performance than the polymer materials. The most commonly used metallic biomaterials for manufacturing stents are nitinol (Ni–Ti), stainless steel (316L SS), cobalt–chromium (Co–Cr) alloy, tantalum (Ta), pure iron (Fe), platinum–iridium (Pt–Ir) alloy, and magnesium (Mg). Ni provides a local immune response and inflammatory reactions. Ta possesses excellent corrosion resistance, but has poor mechanical properties. The material which is used for a stent should not have high magnetic susceptibility because they are not appropriate for magnetic resonance imaging diagnostic in surgeries. There has been increasing research interest in the titanium alloys for the development of metallic stent materials due to their biocompatibility, corrosion resistance, and non-magnetism. Ti–Ta–Hf–Zr (TTHZ) alloys are anticipated to be promising metallic stent materials by virtue of the unique combination of extraordinarily high elastic admissible strain, high mechanical strength, and excellent biocompatibility [18]. X-ray and gamma radiation compatibility of stent alloys are important for radiation diagnosis and therapy aspects. From the detailed literature survey, it is clear that there is no study on the gamma and X-ray radiation compatibility of stent alloys. In the present work, we have studied the gamma and X-ray radiation compatibility of Ti-based alloys such as Ti–37Ta–26Hf–13Zr-24 (wt%) [Alloy 1], Ti–40Ta–22Hf–11.7Zr-26.3 (wt%) [Alloy 2], Ti–45Ta–18.4Hf–10Zr-26.6 (wt%) [Alloy 3], Ti–50Ta–15Hf–8Zr-27 (wt%) [Alloy 4], Ti–55Ta–12Hf–7Zr-26 (wt%) [Alloy 5], and Ti–60Ta–10Hf–5Zr-25 (wt%) [Alloy 6].

2 Theory

2.1 Gamma/X-ray interaction parameters

In the present work, the mass attenuation coefficients (MAC) and photon interaction cross sections in the energy range from 1 keV to 100 GeV are generated using WinXCom [19]. The total linear attenuation coefficient (μ) can be evaluated by multiplying the density of compounds to mass attenuation coefficients.

$$\mu = \left(\frac{\mu}{\rho}\right)_{\mathrm{c}} \times \rho. \tag{1}$$

The total linear attenuation coefficient (μ) is used in the calculation of half-value layer (HVL). HVL is the thickness of an interacting medium that reduces the radiation level by a factor of 2, so to half the initial level, and is calculated by the following equation

$$\mathrm{HVL} = \frac{\ln 2}{\mu} = \frac{0.693}{\mu}. \tag{2}$$

The total linear attenuation coefficient (μ) is also used in the calculation of tenth-value layer (*TVL*). *TVL* is the thickness of the interacting medium for attenuating a radiation beam to 10% of its radiation level and is computed by

$$\mathrm{TVL} = \frac{\ln 10}{\mu} = \frac{2.303}{\mu}. \tag{3}$$

The average distance between two successive interactions is called the relaxation length (λ). It is also called the photon mean free path (MFP), which is determined by the equation

$$\lambda = \frac{\int_0^\infty x \exp(-\mu x)\mathrm{d}x}{\int_0^\infty \exp(-\mu x)\mathrm{d}x} = \frac{1}{\mu}. \tag{4}$$

The gamma interaction parameters, such as linear attenuation coefficients (cm^{-1}), *HVL* (in cm), *TVL* (in cm), and mean free path (in cm), are calculated using Eqs. (1)–(4).

The total molecular cross section, $\boldsymbol{\sigma}_{\mathbf{m}}$ [milli barn], is computed from the following equation using the values of mass attenuation coefficients [$(\mu/\rho)_{\mathrm{c}}$]

$$\sigma_{\mathrm{m}}(E) = \left(\frac{1}{N}\right)\left(\frac{\mu(E)}{\rho}\right)_{\mathrm{c}} \sum_i n_i A_i, \tag{5}$$

where n_i is the number of atoms of ith element in a given molecule, $(\mu/\rho)_{\mathrm{c}}$ is the mass attenuation coefficient of compound, N is the Avogadro's number, and A_{i} is the atomic weight of element i. The effective (average) atomic cross section for a particular atom in the compound σ_{a} [milli barn] is estimated using the equation,

$$\sigma_{\mathrm{a}} = \frac{\sigma_{\mathrm{m}}}{\sum_i n_i} = \frac{\left(\frac{1}{N}\right)\left(\frac{\mu(E)}{\rho}\right)_c \sum_i n_i A_i}{\sum_i n_i} \tag{6}$$

The effective electronic cross section, $\boldsymbol{\sigma}_{\mathbf{e}}$ [milli barn], is computed from the mass attenuation coefficient $(\mu/\rho)_i$ of the ith element in the given molecule using the following equation:

$$\sigma_{\mathrm{e}} = \left(\frac{1}{N}\right) \sum_i \left\{ \left(\frac{f_i A_i}{Z_i}\right) \left(\frac{\mu}{\rho}\right)_i \right\}, \tag{7}$$

where f_i is the fractional abundance (a mass fraction of the ith element in the molecule) and Z_{i} is the atomic number of

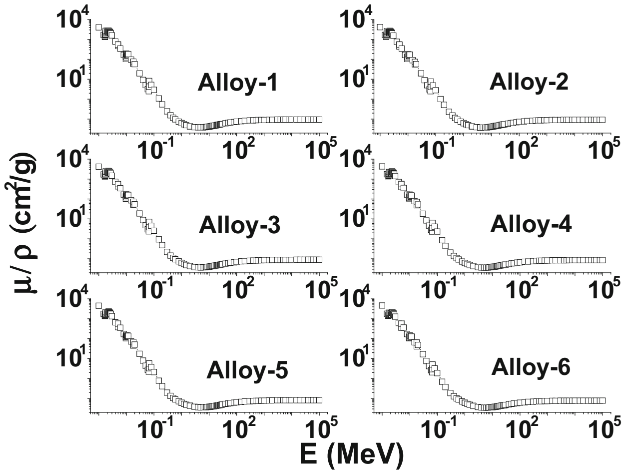

Fig. 1 Variation of total mass attenuation coefficient with photon energy for stent alloys

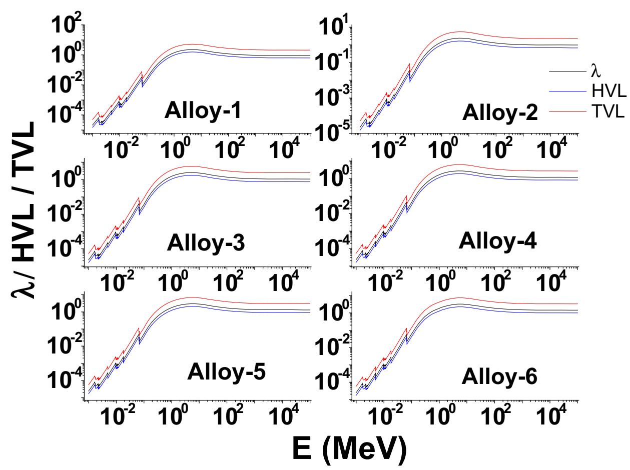

Fig. 2 (Color online) Variation of penetration thickness (mean free path, HVL, and TVL) with energy of photon for stent alloys

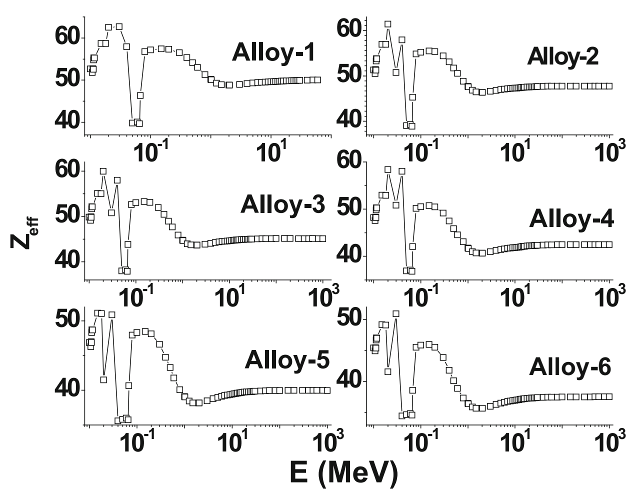

Fig. 3 Variation of effective atomic number with energy of photon for stent alloys

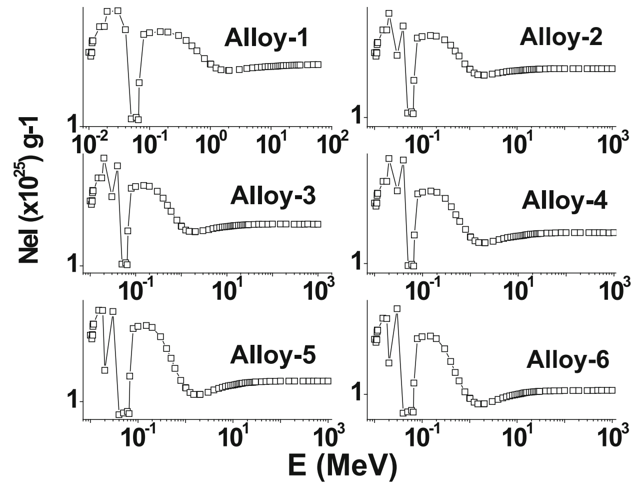

Fig. 4 Variation of effective electron density with energy of photon for stent alloys

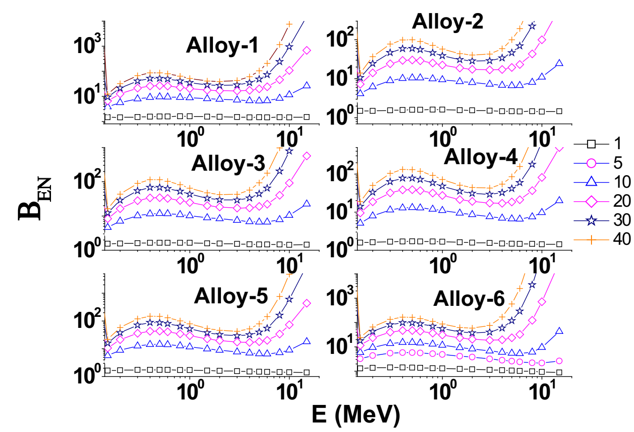

Fig. 5 (Color online) Variation of exposure buildup factors with energy of photon for stent alloys

the ith element in a molecule. Finally the Z_{eff} is estimated as

$$Z_{\mathrm{eff}} = \frac{\sigma_a}{\sigma_e}. \tag{8}$$

The effective electron density (N_e), expressed in terms of number of electrons per unit mass, is closely related to the effective atomic number. For an element, the electron density is given by $N_e = NZ/A$ [electrons/g]. This expression can be generalized for a compound using

$$N_e(g^{-1}) = \frac{N}{\sum_i n_i A_i} Z_{\mathrm{eff}} \sum_i n_i. \tag{9}$$

2.2 Secondary radiation during the interaction of gamma/X-ray

During the interaction of gamma/X-rays with the medium, it degrades their energy and produces secondary radiations through the different interaction process. The quantity of secondary radiations produced in the medium and energy deposited/absorbed in the medium is studied by calculating buildup factors. In the present work, we have estimated energy exposure buildup factors (B_{en}) using G–P fitting method [20–22]. We have evaluated the G–P fitting parameters (*b, c, a,* X_k, and *d*) for different stent alloys using the following expression, which is based on Lagrange's interpolation technique

$$P_{Z_{\mathrm{eff}}} = \sum \left(\frac{\prod_{Z' \neq Z} (Z_{\mathrm{eff}} - Z)}{\prod_{z \neq Z} (z - Z)} \right) P_z, \tag{10}$$

where lowercase z is the atomic number of the element of known G–P fitting parameter, P_z is adjacent to the effective atomic number (Z_{eff}) of the given material of known whose G–P fitting parameter, $P_{Z_{\mathrm{eff}}}$ is desired, and uppercase Z is the atomic numbers of other elements of known G–P fitting parameter adjacent to Z_{eff}. G–P fitting parameters (*b, c, a,* X_k, and *d*) for elements adjacent to Z_{eff} are provided by the standard data available in the literature [23]. The computed G–P fitting parameters (*b, c, a,* X_k, and *d*) were then used to compute the EABF in the energy range 0.015–15 MeV up to a penetration depth of 40 mean free path with the help of G–P fitting formula, as given by the equations

$$B(E,X) = 1 + \frac{b-1}{K-1}(K^X - 1) \quad \text{for } K \neq 1, \tag{11}$$

$$B(E,X) = 1 + (b-1)X \quad \text{for } K = 1, \tag{12}$$

$$K(E,X) = CX^{\mathrm{a}} + d\,\frac{\tanh\left(\frac{X}{X_K} - 2\right) - \tanh(-2)}{1 - \tanh(-2)} \tag{13}$$

For penetration depth $(X) \leq 40$ mfp,

where X is the source–detector distance for the medium in mean free paths (mfp), b is the value of buildup factor at 1 mfp, $K(E, X)$ is the dose multiplication factor, and *b, c, a,* X_k, and *d* are computed G–P fitting parameters that depend on attenuating medium and source energy.

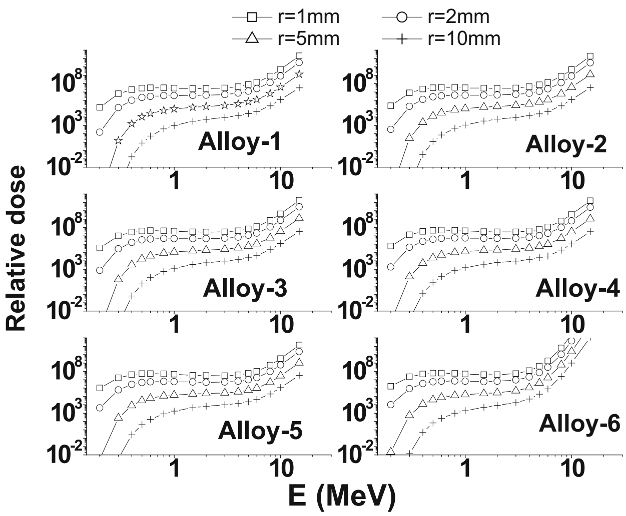

Fig. 6 Variation of relative dose with energy of photon for stent alloys

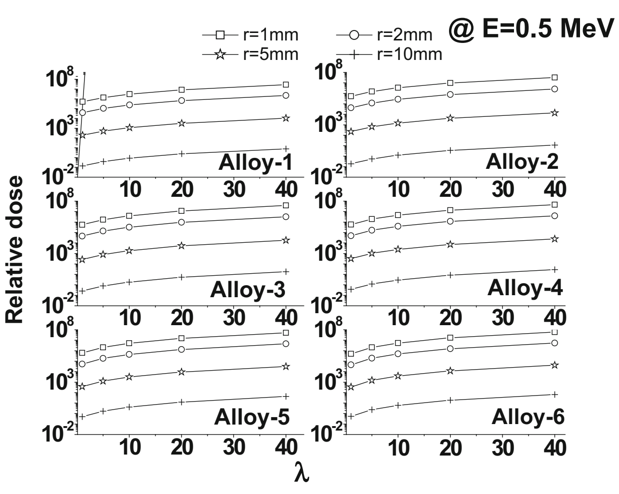

Fig. 7 Variation of relative dose with penetration depth for stent alloys

2.3 Relative dose

The radial dependence of dose is $e^{-\mu r}B/r^2$, where μ denotes the linear attenuation coefficient for the appropriate photon energy, and B is the exposure buildup factor. Dose distribution at a distance r is given by [21]

$$D_{\mathrm{r}} = D_0 e^{-\mu \times r} B/r. \tag{14}$$

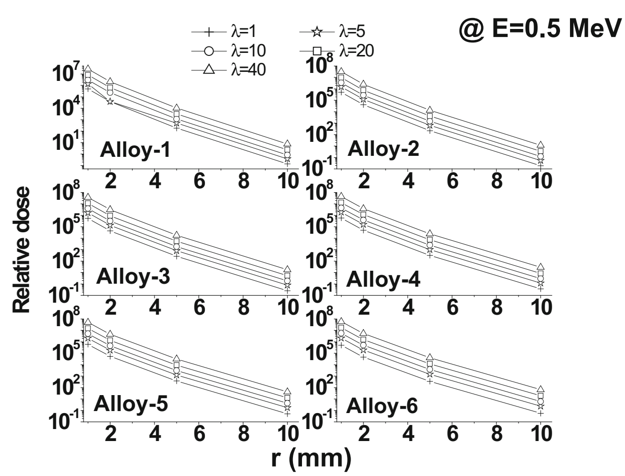

Fig. 8 Variation of relative dose with thickness of the medium for stent alloys

Table 1 Comparison of total mass attenuation coefficient, mean free path, *HVL*, *TVL*, and effective electron density of stent alloys with that of arteries and veins

Energy (MeV)	0.01	0.02	0.05	0.1	0.2	0.5	1	2	5	10
μ/ρ (cm^2/g)										
Arteries	16.492	2.365	0.328	0.182	0.138	0.096	0.070	0.049	0.031	0.023
Alloy 1	180.262	56.974	5.033	2.953	0.546	0.116	0.063	0.043	0.038	0.042
Alloy 2	169.852	56.175	4.944	2.757	0.515	0.114	0.063	0.043	0.037	0.041
Alloy 3	167.193	54.601	4.787	2.543	0.481	0.111	0.062	0.043	0.037	0.040
Alloy 4	158.086	52.841	4.611	2.296	0.442	0.107	0.062	0.043	0.036	0.039
Alloy 5	137.080	50.683	4.404	2.082	0.409	0.105	0.061	0.043	0.035	0.038
Alloy 6	142.943	48.311	4.175	1.842	0.371	0.101	0.061	0.042	0.035	0.036
λ (cm)										
Arteries	1.19E−1	7.80E−1	2.87E+0	3.86E+0	4.81E+0	6.81E+0	9.32E+0	1.33E+1	2.18E+1	2.98E+1
Alloy 1	4.69E−4	1.48E−3	1.68E−2	2.86E−2	1.55E−1	7.26E−1	1.34E+0	1.96E+0	2.25E+0	2.03E+0
Alloy 2	5.22E−4	1.58E−3	1.79E−2	3.22E−2	1.72E−1	7.80E−1	1.42E+0	2.06E+0	2.39E+0	2.18E+0
Alloy 3	5.60E−4	1.72E−3	1.96E−2	3.68E−2	1.95E−1	8.45E−1	1.51E+0	2.18E+0	2.56E+0	2.36E+0
Alloy 4	6.31E−4	1.89E−3	2.16E−2	4.35E−2	2.26E−1	9.29E−1	1.62E+0	2.33E+0	2.78E+0	2.58E+0
Alloy 5	7.77E−4	2.10E−3	2.42E−2	5.12E−2	2.60E−1	1.02E+0	1.74E+0	2.50E+0	3.01E+0	2.83E+0
Alloy 6	7.94E−4	2.35E−3	2.72E−2	6.16E−2	3.06E−1	1.12E+0	1.86E+0	2.67E+0	3.27E+0	3.11E+0
HVL (cm)										
Arteries	1.72E−1	1.13E+0	4.14E+0	5.56E+0	6.94E+0	9.82E00	1.35E+1	1.93E+1	3.14E+1	4.30E+1
Alloy 1	3.25E−4	1.03E−3	1.16E−2	1.98E−2	1.07E−1	5.03E−1	9.31E−1	1.36E+0	1.56E+0	1.41E+0
Alloy 2	3.62E−4	1.09E−3	1.24E−2	2.23E−2	1.19E−1	5.41E−1	9.83E−1	1.43E+0	1.66E+0	1.51E+0
Alloy 3	3.88E−4	1.19E−3	1.36E−2	2.55E−2	1.35E−1	5.86E−1	1.04E+0	1.51E+0	1.77E+0	1.63E+0
Alloy 4	4.37E−4	1.31E−3	1.50E−2	3.01E−2	1.56E−1	6.44E−1	1.12E+0	1.62E+0	1.92E+0	1.79E+0
Alloy 5	5.38E−4	1.46E−3	1.68E−2	3.55E−2	1.81E−1	7.06E−1	1.20E+0	1.73E+0	2.09E+0	1.96E+0
Alloy 6	5.50E−4	1.63E−3	1.88E−2	4.27E−2	2.12E−1	7.76E−1	1.29E+0	1.85E+0	2.26E+0	2.16E+0
TVL (cm)										
Arteries	3.97E−1	2.59E+0	9.55E+0	1.28E+1	1.60E+1	2.26E+1	3.10E+1	4.43E+1	7.23E+1	9.89E+1
Alloy 1	1.08E−3	3.42E03	3.87E−2	6.59E−2	3.57E−1	1.67E+0	3.09E+0	4.51E+0	5.18E+0	4.69E+0
Alloy 2	1.20E−3	3.64E−3	4.13E−2	7.41E−2	3.97E−1	1.80E+0	3.27E+0	4.75E+0	5.50E+0	5.02E+0
Alloy 3	1.29E−3	3.95E−3	4.50E−2	8.48E−2	4.48E−1	1.95E+0	3.47E+0	5.03E+0	5.90E+0	5.42E+0
Alloy 4	1.56E−3	4.35E−3	4.98E−2	1.00E−1	5.19E−1	2.14E+0	3.72E+0	5.38E+0	6.39E+0	5.94E+0
Alloy 5	1.79E−3	4.84E−3	5.57E−2	1.18E−1	6.00E−1	2.35E+0	4.00E+0	5.75E+0	6.93E+0	6.52E+0
Alloy 6	1.83E−3	5.41E−3	6.26E−2	1.42E−1	7.04E−1	2.58E+0	4.29E+0	6.15E+0	7.52E+0	7.17E+0
Nel ($g^{-1} \times 10^{25}$)										
Arteries	0.600	0.580	0.390	0.340	0.330	0.330	0.330	0.330	0.340	0.360
Alloy 1	1.366	1.622	1.032	1.482	1.487	1.404	1.301	1.265	1.279	1.286
Alloy 2	1.342	1.606	1.020	1.444	1.447	1.353	1.246	1.212	1.228	1.237
Alloy 3	1.322	1.591	1.008	1.406	1.408	1.298	1.187	1.158	1.174	1.184
Alloy 4	1.295	1.568	0.991	1.357	1.356	1.232	1.121	1.092	1.113	1.124
Alloy 5	1.258	1.114	0.961	1.297	1.292	1.162	1.050	1.025	1.047	1.059
Alloy 6	1.227	1.124	0.936	1.239	1.230	1.084	0.986	0.964	0.987	0.999

Here D_0 is the initial dose delivered by the point gamma ray emitter. The relative dose distribution at a distance r is

$$\frac{D_r}{D_0} = e^{-\mu \times r} B/r. \tag{15}$$

Hence, the relative dose distribution can be evaluated using estimated exposure buildup for different penetration depths.

3 Results and discussions

The calculated mass attenuation coefficient for Stent alloys is graphically represented in Fig. 1. Mass attenuation coefficient values for Stent alloys are large in the low-energy region and decrease progressively. Variation of the mass attenuation coefficient with incident photon energy can be explained on the basis of different photon interaction processes such as the photoelectric process, Compton scattering, and pair production. In the low-energy region, the mass attenuation coefficient is observed to be high due to the dominant photoelectric interaction. In the high-energy region, Compton scattering becomes dominant and depends linearly with atomic number. Hence, mass attenuation coefficient value becomes the minimum value.

The calculated HVL, TVL, and MFP for different incident energies of Stent alloys are graphically represented in Fig. 2. All these parameters increase progressively with an increase in photon energy up to few keV (250 keV) due to dominant photoelectric absorption; beyond this energy, these parameters increase slowly (up to 6 MeV) with energy due to Compton scattering. After 6 MeV, these parameters remain almost constant with energy due to pair production. The variation of effective atomic number with energy for stent alloys is shown in Fig. 3. The effective atomic number values for Stent alloys are large in the low-energy region (due to photoelectric effect) and decrease progressively, thereafter increases and becomes constant for high energy (due to pair production). Similar variations are observed in the case of effective electron density and shown in Fig. 4.

The variation of energy exposure buildup factor (EBF) for stent alloys is shown in Fig. 5. It is observed that EBF increases up to the E_{pe} and then decreases. Here, E_{pe} is the energy value at which the photoelectric interaction coefficients match with Compton interaction coefficients for a given value of effective atomic number (Z_{eff}). The variation of EBF with energy is due to the dominance of photoelectric absorption in the lower end and dominance of pair production in the higher-photon energy region. Similar variations are observed in cases of variation of relative dose with energy and are shown in Fig. 6. The variation of relative dose with mean free path for stent alloys at 0.5 MeV for different thickness of the medium (1, 2, 5, 10 mm) is shown in Fig. 7. Relative dose values increase with an increase in mean free path. As mean free path increases, thickness of the interacting material increases, which results in an increase in scattering events. Hence, it results in large relative dose values.

The variation of relative dose with thickness of the medium for stent alloys at 0.5 MeV for different mean free paths (1, 5, 10, 20, and 40) is shown in Fig. 8. The computed relative dose decreases with an increase in the thickness of the medium. As the thickness of the medium increases, energy of incident gamma/X-ray decreases due to scattering or absorption. Hence, it results in a decreasing trend of relative dose with an increase in thickness of the medium.

Coronary stents are small, expandable tubes made up of alloys that are implanted in the arteries. To test the gamma and X-ray radiation compatibility of Ti–Ta–Hf–Zr alloys for coronary stent applications, we have compared gamma/X-ray radiation interaction parameters such as mass attenuation coefficient, mean free path, *HVL*, *TVL*, and effective electron density of Ti–Ta–Hf–Zr alloys with that of arteries. This comparison is shown in Table 1. Among the studied alloys, gamma and X-ray interaction parameters for alloy 5 [Ti–55Ta–12Hf–7Zr-26 (wt%)] and alloy 6 [Ti-60Ta–10Hf–5Zr-25 (wt%)] are nearly close to that of arteries. Thus, among the studied Ti–Ta–Hf–Zr alloys, Ti-55Ta–12Hf–7Zr-26 and Ti–60Ta–10Hf–5Zr-25 are gamma and X-ray radiation compatible than the other studied alloys. The alloys Ti–55Ta–12Hf–7Zr-26 and Ti–60Ta–10Hf–5Zr-25 have added properties such as radiation compatibility including high elastic admissible strain, high mechanical strength, and excellent biocompatibility [18]. Hence, we may suggest that, among Ti–Ta–Hf–Zr alloys, these alloys are the best materials for coronary stent applications.

References

1. C. Vasilescu, P. Osiceanu, J.M. Calderon Moreno et al., Microstructure, surface characterization and long-term stability of new quaternary Ti–Zr–Ta–Ag alloy for implant use. Mater. Sci. Eng. **71**(1), 322–334 (2017). https://doi.org/10.1016/j.msec.2016.10.004
2. P.V. Sreenivasa Reddy, V. Kanchana, Ab initio study of Fermi surface and dynamical properties of Ni_2XAl (X = Ti, V, Zr, Nb, Hf and Ta). J. Alloys Compd. **616**(15), 527–534 (2014). https://doi.org/10.1016/j.jallcom.2014.07.020
3. X.H. Zheng, J.H. Sui, X. Zhang et al., Thermal stability and high-temperature shape memory effect of Ti–Ta–Zr alloy. Scr. Mater. **68**(12), 1008–1011 (2013). https://doi.org/10.1016/j.scriptamat.2013.03.008
4. P. Stenlund, O. Omar, U. Brohede et al., Bone response to a novel Ti–Ta–Nb–Zr alloy. Acta Biomater. **20**(1), 165–175 (2015). https://doi.org/10.1016/j.actbio.2015.03.038
5. Y.F. Xu, Y.F. Xiao, D.Q. Yi et al., Corrosion behavior of Ti–Nb–Ta–Zr–Fe alloy for biomedical applications in Ringer's solution. Trans. Nonferr. Metal. Soc. **25**(8), 2556–2563 (2015). https://doi.org/10.1016/S1003-6326(15)63875-4
6. X.M. Ma, W. Sun, Characterization of deformation localization in cold-rolled metastable β-Ti–Nb–Ta–Zr alloy. J. Alloys Compd. **509**(1), S294–S298 (2011). https://doi.org/10.1016/j.jallcom.2011.01.084
7. F. Zhang, Z. Yu, C. Xiong et al., Martensitic transformations and the shape memory effect in Ti–Zr–Nb–Al high-temperature shape

memory alloys. Mater. Sci. Eng., A **679**(2), 14–19 (2017). https://doi.org/10.1016/j.msea.2016.10.023
8. H.J. Kim, Y.H. Jeong, H.C. Choe et al., Hydroxyapatite formation on biomedical Ti–Ta–Zr alloys by magnetron sputtering and electrochemical deposition. Thin Solid Films **572**(1), 119–125 (2014). https://doi.org/10.1016/j.tsf.2014.07.058
9. X. Song, L. Wang, M. Niinomi et al., Microstructure and fatigue behaviors of a biomedical Ti–Nb–Ta–Zr alloy with trace CeO_2 additions. Mater. Sci. Eng., A **619**(1), 112–118 (2014). https://doi.org/10.1016/j.msea.2014.09.069
10. L.S. Wei, H.Y. Kim, S. Miyazaki, Effects of oxygen concentration and phase stability on nano-domain structure and thermal expansion behavior of Ti–Nb–Zr–Ta–O alloys. Acta Mater. **100**, 313–322 (2015). https://doi.org/10.1016/j.actamat.2015.08.054
11. L.M. Elias, S.G. Schneider, S. Schneider et al., Microstructural and mechanical characterization of biomedical Ti–Nb–Zr(–Ta) alloys. Mater. Sci. Eng., A **432**(1–2), 108–112 (2006). https://doi.org/10.1016/j.msea.2006.06.013
12. Y.H. Jeong, W.G. Kim, H.C. Choe et al., Control of nanotube shape and morphology on Ti–Nb(Ta)–Zr alloys by varying anodizing potential. Thin Solid Films **572**(1), 105–112 (2014). https://doi.org/10.1016/j.tsf.2014.09.057
13. N. Sakaguchi, M. Niinomi, T. Akahori et al., Relationships between tensile deformation behavior and microstructure in Ti–Nb–Ta–Zr system alloys. Mater. Sci. Eng., C **25**(3), 363–369 (2005). https://doi.org/10.1016/j.msec.2004.12.014
14. J. Málek, F. Hnilica, J. Veselý et al., The influence of chemical composition and thermo-mechanical treatment on Ti–Nb–Ta–Zr alloys. Mater. Design **35**, 731–740 (2012). https://doi.org/10.1016/j.matdes.2011.10.030
15. Y.F. Xu, D.Q. Yi, H.Q. Liu et al., Effects of cold deformation on microstructure, texture evolution and mechanical properties of Ti–Nb–Ta–Zr–Fe alloy for biomedical applications. Mater. Sci. Eng., A **547**, 64–71 (2012). https://doi.org/10.1016/j.msea.2012.03.081
16. Q. Wei, L. Wang, Y. Fu et al., Influence of oxygen content on microstructure and mechanical properties of Ti–Nb–Ta–Zr alloy. Mater. Design **32**(5), 2934–2939 (2011). https://doi.org/10.1016/j.matdes.2010.11.049
17. C. Vasilescu, S.I. Drob, P. Osiceanu et al., Microstructure, surface characterization, and electrochemical behavior of new Ti–Zr–Ta–Ag alloy in simulated human electrolyte. Metall. Mater. Trans. A **48**(1), 513–523 (2017). https://doi.org/10.1007/s11661-016-3774-2
18. J. Lin, S. Ozan, Y. Li et al., Novel Ti–Ta–Hf–Zr alloys with promising mechanical properties for prospective stent applications. Sci. Rep. **6**, 37901 (2016). https://doi.org/10.1038/srep37901
19. L. Gerward, N. Guilbert, K.B. Jensen et al., WinXCom—a program for calculating X-ray attenuation coefficients. Radiat. Phys. Chem. **71**, 653–654 (2004). https://doi.org/10.1016/j.radphyschem.2004.04.040
20. H.C. Manjunatha, B. Rudraswamy, Energy absorption and exposure build-up factors in hydroxyapatite. Radiat. Meas. **47**(5), 364–370 (2012). https://doi.org/10.1016/j.radmeas.2012.02.001
21. H.C. Manjunatha, B. Rudraswamy, Computation of exposure build-up factors in teeth. Radiat. Phys. Chem. **80**(1), 14–21 (2011). https://doi.org/10.1016/j.radphyschem.2010.09.004
22. H.C. Manjunatha, B. Rudraswamy, Energy absorption build-up factors in teeth. J. Radioanal. Nucl. Chem. **294**(2), 251–260 (2012). https://doi.org/10.1007/s10967-011-1490-3
23. American National Standard (ANS Gamma-ray attenuation coefficients and buildup factor for engineering materials. ANSI/ANS 6.4.3.) 1991. Article ID: 240180